

Strongly coupled magneto-exciton condensates in large-angle twisted double bilayer graphene

Qingxin Li^{1†}, Yiwei Chen^{1†}, LingNan Wei^{1†}, Hong Chen^{1†}, Yan Huang¹, Yujian Zhu¹, Wang Zhu¹, Dongdong An¹, Junwei Song¹, Qikang Gan¹, Qi Zhang¹, Kenji Watanabe², Takashi Taniguchi³, Xiaoyang Shi⁴, Kostya S. Novoselov⁵, Rui Wang^{1*}, Geliang Yu^{1*}, and Lei Wang^{1*}

¹*National Laboratory of Solid-State Microstructures,*

School of Physics, Nanjing University, Nanjing, 210093, China

²*Research Center for Electronic and Optical Materials,*

National Institute for Materials Science, 1-1 Namiki, Tsukuba 305-0044, Japan.

³*Research Center for Materials Nanoarchitectonics,*

National Institute for Materials Science, 1-1 Namiki, Tsukuba 305-0044, Japan

⁴*Department of Earth and Environmental Engineering,*

Columbia University, New York, NY 10027, USA

⁵*Institute for Functional Intelligent Materials, National University of Singapore,*

Building S9, 4 Science Drive 2, Singapore, 117544

[†]*These authors contributed equally to this work. and*

** Corresponding authors, Email: ruiwang@nju.edu.cn; yugeliang@nju.edu.cn; leiwang@nju.edu.cn*

Excitons, the bosonic quasiparticle emerging from Coulomb interaction between electrons and holes, will undergo a Bose-Einstein condensation (BEC) and transition into a superfluid state with global phase coherence at low temperatures. An important platform to study such excitonic physics is built on double-layer quantum wells or recent two-dimensional material heterostructures, where two parallel planes of electrons and holes are separated by a thin insulating layer. Lowering this separation distance (d) enhances the interlayer Coulomb interaction thereby strengthens the exciton binding energy. However, an exceedingly small d will lead to the undesired interlayer tunneling, which results the annihilation of excitons. Here, we report the observation of a sequences of robust exciton condensates (ECs) in double bilayer graphenes twisted to $\sim 10^\circ$ with no insulating mid-layer. The large momentum mismatch between the two graphene layers well suppress the interlayer tunneling, allowing us to reach the separation lower limit ~ 0.334 nm and investigate ECs in the extreme coupling regime. Carrying out transport measurements on the bulk and edge of the devices, we find incompressible states corresponding to ECs when both layers are half-filled in the $N = 0$ and $N = 1$ Landau levels (LLs). The comparison between these ECs and theoretical calculations suggest that the low-energy charged excitation of ECs can be meron-antimeron or particle-hole pair, which relies on both LL index and carrier type. Our results establish large-angle twisted bilayers as an experimental platform with extreme coupling strength for studying quantum bosonic phase and its low-energy excitations.

An EC is a Bose-Einstein condensate formed when

a large number of electron-hole pairs occupy the ground state with macroscopic phase coherence [1]. In bulk materials, condensed excitons can be generated by optical pumping but with short lifetimes [2]. In small-bandgap semiconductors and semimetals, ECs are predicted to live for longer time whereby exciton binding energy exceeds the charge gap [3]. But the structural character of spontaneous symmetry breaking in these solid-state systems may hamper the possibility to realize superfluidity [4, 5]. Double-layer system subject to finite magnetic field is shown as impressive platform for exciton condensation [6, 7]. As the recombination is blocked by mid-layer insulator, electron-like carriers in a partially filled LL in one layer couple with hole-like carriers in the other, forming interlayer magneto-excitons, which then experience a Bose-Einstein condensation to a coherent superfluid ground state [8–11].

The energy of the magneto-excitons is determined by the ratio of intralayer and the interlayer Coulomb interaction: $E_{intra}/E_{inter} \sim d/l_B$, where $l_B = \sqrt{\hbar/eB}$ is the magnetic length, \hbar is the reduced Planck constant, e is electron charge, and B is magnetic field. An attractive characteristic of such quantum hall bilayer structure is that d/l_B can be tuned by B and d , providing an opportunity to adjust the electron-hole coupling strength and average distance between excitons. In this way, it facilitates exploring quantum condensate phase changes in bosonic system, e.g., the crossover of weak-coupling Bardeen-Cooper-Schrieffer (BCS) pairing to a strong-coupling BEC pairing [12] and the transition of superfluid coherent phase to translational symmetry breaking supersolid coherent phase [13]. However, the intriguing region with extremely strong coupling which needs tiny d/l_B remains elusive due to the difficulty in achieving extremely small d without raising interlayer tunneling.

Recently, progress on reducing the d down to sub-

nanometer has been made in natural bilayer WSe_2 , where interlayer tunneling was avoided by the intrinsic spin-valley structure [14]. However, the unipolar nature of such semiconductor system limits the observation of magneto-excitons only on the hole side. Another candidate reaching such a small d is the large-angle twisted graphene system, where a large momentum mismatch between different sheets suppresses the interlayer tunneling [15], making it possible to realize ECs in the strong coupling limit with layers widely covering both the electron and hole sides. Although recent studies have shown some plausible traces of ECs in such twisted bilayers by observing quantum Hall states (QHSs) at some incomplete odd-integer total fillings limited on one carrier side [16, 17], due to contact quality issues and disorders [16], the sequence of ECs is yet to be observed.

Here, we reported the observation of a complete sequence of ECs emerging at both electron and hole fillings with extremely strong coupling strength in high quality large twisted angle twisted double bilayer graphene (TDBG) devices (FIG. 1a). At finite magnetic field, the interlayer tunneling gap due to spatial wave functions overlap in two bilayers can be negligible (10^{-10} meV) based on our numerical calculation (see Supplementary Information section 4). By measuring the bulk and edge transport properties, we unambiguously identified these robust ECs which appear at the half-filled $N = 0$ and $N = 1$ LL. Thermally activated measurements combined with theoretical models indicate that the low-energy charged excitation of ECs is topologically nontrivial spin-texture in $N = 0$ LL [18], whereas for $N = 1$ LL, it changes from such spin-texture on the hole side to particle-hole pair on the electron side.

We fabricated high-quality TDBG devices with ‘cut and pick-up’ transfer method [19, 20] by picking up and twisting two pieces of bilayer graphene, cut from a single flake, to an angle about 10° . (see in Supplementary Information section 1). Depicted in FIG. 1b, the structure of device, which contains top and bottom graphite gates with voltages V_T and V_B , allows us to independently tune carrier density: $n = (C_B V_B + C_T V_T)/e$, and displacement field: $D = (C_B V_B - C_T V_T)/2$, where $C_T (C_B)$ is top (bottom) gate capacitance and e is the elementary charge. FIG. 1c shows the longitudinal resistance R_{xx} as a function of n and D in the absence of a magnetic field. A high resistance state appearing around zero values of n and D suggests the presence of crystal fields [15], which occurs due to the imbalance of electron occupancy between the outer two layers and inner ones. Upon increasing the displacement field, the high resistance state evolves into two splitting resistive traces, dividing the diagram for $D > 0$ into five regions (FIG. 1d), which correspond to the different carrier population configurations in the two bilayers. In region I and V, both bilayers are simultaneously

populated by either holes or electrons respectively; in region II and IV, one of the bilayers is gapped while the other is filled; in region III, the two bilayers are populated by opposite carrier types and the system contains a mixture of holes and electrons. This layer-selective population behavior evidences the two bilayers in our large-angle TDBG are decoupled, allowing the top and bottom gates to control them separately [21, 22]. (Supplementary Information section 2).

Next, we investigate the behavior of system under magnetic fields. FIG. 1f plots the R_{xx} versus the D and total filling factor ν_{tot} at $B = 14\text{T}$, where $\nu_{tot} = \nu_T + \nu_B$, and ν_T, ν_B are the LL filling fractions of the top and bottom bilayer respectively. In bilayer graphene (BLG), the zero-energy LL (ZLL) has eight-fold degeneracy (spin, valley, and accidental orbital degeneracy $N = 1, N = 0$) and higher LLs have four-fold degeneracy [23]. As for our system consisting of two decoupled bilayer graphene layers, LLs have an extra two-fold degeneracy corresponding to ‘top layer’ and ‘bottom layer’ regulated by D . At $B = 14\text{T}$, these degeneracies are fully lifted, showing a sequence of QHSs at all integer fillings as resistance minima lines paralleling to the $n = 0$ line. Strikingly, we observed some repeated ‘ 4×4 ’ matrices (for $|\nu_{tot}| > 8$) and a unique ‘ 8×8 ’ matrix (for $-8 < \nu_{tot} < 8$). These matrices can be qualitatively understood using the single-particle picture of LL crossings as illustrated in FIG. 1e and FIG. 1g. In a ‘ 4×4 ’ matrix, along the white dashed line (FIG. 1f) at $D = 0$, four QHSs at even total fillings stabilized by the spin and valley degeneracy lifting. As $|D|$ increases, the layer degeneracy is lifted and each of these four LLs splits into two, subsequently intersect with their neighbors, forming a series of crossing points (marked by yellow circles in FIG. 1g). At these crossing points, the double bilayer system is gapless since both bilayers are in partially filled LLs (more details in Supplementary Information section 3).

Now we move on to look into the ‘ 8×8 ’ matrix centered at the charge neutrality point. In FIG. 2a we plot longitudinal conductance σ_{xx} versus D and ν_{tot} for $-9 < \nu_{tot} < 9$. A clear ‘ 8×8 ’ structural pattern with a forming mechanism analogous to the ‘ 4×4 ’ matrices is displayed, which corresponds to crossings of the quantum Hall octet from two decoupled bilayers (schematically illustrated in FIG. 2c). Unexpectedly, focusing on $D = 0\text{V/nm}$, we notice a series of exceptional crossing points at $\nu_{tot} = -7, -3, -1, 1, 3$ and 5 (red dotted circles in FIG. 2a and FIG. 2c) manifesting as anomalous states with quantized Hall conductivity and vanishing longitudinal conductivity, which is drastic contrast to the finite conductivity in those normal LL crossings. (see FIG. S4). Besides, for $D \neq 0$, a few similar anomalous states also develop with the reduced longitudinal conductivity marked by orange dotted circles in FIG. 2a. These anomalous states are inadequate to be understood from the

single-particle LL crossings picture, where the system should show a finite conductivity as both bilayer LLs are half-filled.

In order to investigate the origin of the vanishing of σ_{xx} at these crossing points, we further measure the bulk transport properties of these anomalous states using the configuration shown in FIG. 2b inset [24]. FIG. 2b maps the bulk resistance $R_{xx-Bulk}$ as a function of ν_{tot} and D on the same ‘ 8×8 ’ matrix. Along $D = 0$ V/nm, each anomalous state manifests a high $R_{xx-Bulk}$ peak while other LL crossings show $R_{xx-Bulk}$ dips. Based on these two different patterns of $R_{xx-Bulk}$ at the crossing points, we group them into three categories as shown in FIG. 2d, e, f. In top panels, the center of these $R_{xx-Bulk}(\nu_{tot}, D)$ maps corresponds to both bilayers are half-filled and we take linecuts at the crossing points showing $R_{xx-Bulk}$ vs ν_{tot} in bottom panels. For normal crossing points (FIG. 2d), the resistance dip in $R_{xx-Bulk}$ linecut manifests that the system is compressible at these states. This confirms the single-particle LL crossings picture, meanwhile, also indicates the tunneling is negligible between two bilayers otherwise a LL anti-crossing gap would be induced by tunneling [25, 26]. On the contrary, for the anomalous crossing points along $D = 0$ (FIG. 2e), the prominent resistive peak demonstrates the state is incompressible which is beyond the picture of single-particle LL crossing. Given that the tunneling is negligible here, this phenomenon implies the emergence of a correlation energy gap due to many-body interactions. When both bilayers are half-filled, interlayer interactions prompt electrons in one bilayer and holes in the other to form magneto-excitons [10, 11] and condense into an incompressible superfluid: exciton condensate. Besides, it’s worth pointing out that the crossing points for $D \neq 0$ (FIG. 2f) show comparatively weaker bulk-resistance peak compared to those along $D = 0$. This is presumably due to the imbalanced occupancy of LL orbitals of top and bottom bilayers [13, 27] or slight spatial wave functions overlap in two bilayers induced by finite D .

To characterize the ECs, we examined the excitation energy gap at all odd-integer filling for $-8 < \nu_{tot} < 8$ with thermal activation measurements. FIG. 3a shows temperature dependence of bulk resistance ($R_{xx-Bulk}$) as a function of ν_{tot} at $D = 0$ V/nm for $B = 14$ T. The EC gap (Δ) shows an unexpected hierarchy and manifests as a nonmonotonic behavior with ν_{tot} (FIG. 3c). Remarkably, all ECs appear in $-4 < \nu_{tot} \leq 4$ hold obviously larger gap value than those appear in other odd-integer fillings. In BLG, orbital character of the ZLL has been mapped out as the function of filling factors and electric fields [27], and the holes or electrons are fully polarized in a single orbital component ($N = 0$ or 1) covering the whole of accessible parameter space. Based on this picture, we displayed the distribution of orbital index

of these two decoupled bilayers with filling factors under strong magnetic field in FIG. 3b. Near $D \approx 0$, LLs of both bilayers with unambiguous orbital index cross with each other, giving rise to the filling sequence of orbital index throughout $-8 \leq \nu_{tot} \leq 8$ as: $-4 < \nu_{tot} \leq 0$, $4 \leq \nu_{tot} \leq 8$ corresponds to $N = 1$ LL and $-8 \leq \nu_{tot} < -4$, $0 \leq \nu_{tot} < 4$ are in accord with $N = 0$ LL. As a result, we find that the EC robustness is tightly associated with LL index and carrier type (electron-hole asymmetry), specifically, ECs appearing within the $N = 1$ orbital of hole side are more stable than those within the $N = 0$ orbital whereas it is opposite on the electron side.

The orbital wavefunction plays an important role for formation of correlated states. For example, in BLG, compared to the conventional $N = 0$ orbital with sharper composite-fermion interactions, the $N = 1$ orbital has softer interactions which are beneficial for pairing due to an additional node in the single-particle wavefunction [28], and that lead to the observation of the even-denominator fractional QHSs exclusively within LL $N = 1$, not $N = 0$. [29–32]. For our system consisting of two decoupled bilayers, different orbitals may host distinct low energy excitations, which affects the robustness of ECs. This influence can be better understood by taking pseudospin magnetism picture into consideration in which pseudospin up (down) corresponds to an electron or a hole in the upper(lower) bilayer, and spontaneous-interlayer-coherence broken symmetry occurs as easy-plane pseudo-ferromagnetism [18]. In this case, considering the finite interlayer spacing d , topologically stable charged vortices known as meron can emerge. [18, 33] Then the merons and anti-merons pairing, leads to the topologically nontrivial spin configurations known as skyrmions. Theoretical works have suggested that the energy of this excitation increases with orbital index n [34]. The meron-antimeron spin-texture is not the sole low-energy excitation in the double-layer system. With increasing of LL orbital index, conventional particle-hole pairs may host lower energy due to shorter-ranged interactions caused by excessive screening, and overtakes meron-antimeron pairs. A recent study suggests that in p-type bilayer WSe₂ the spin-texture charged excitation only occurs in LLs $n \leq 2$ [14], while higher Landau levels host the particle-hole excitation whose energy decreases with orbital index n .

In our TDBG system, theoretical calculations suggest that the low-energy charged excitation of ECs is not only related to LL index but also associated with carrier doping type. FIG. 3d shows the theoretical calculation of the $\Delta - N$ (LL index) dependence of these two different charged excitations. It reveals that the spin-texture charged excitations for ECs are favoured in the lower LLs on both electron and hole sides, and switch to particle-hole type at higher LL index. However, the transition points between two

types of charged excitations are different on electron and hole sides, with the EC-gap maximum occurring between $N = 1$ and $N = 2$ for hole side and near $N = 0$ for electron side. This discrepancy can be well understood by considering the different screening strength between the hole and electron sides. Being in ZLL of TDBG at $D = 0$, with the total filling increasing, carriers populate QHSs with different spin-valley flavour from $\nu_{tot} = -8$ to 8 sequentially. At the same time, increasing particle density strengthens the screening, driving a shorter-ranged interaction. This, in turn, reduces the excitation energy of particle-hole pair originating from exchange interactions, whereas leaving the spin-texture excitation energy unaffected. This theoretical result well agrees with our observed EC-gap trend. On the hole side, ECs in $N = 1$ and $N = 0$ hold spin-texture excitations, thereby excitation energies monotonically increase with the LL index. Meanwhile, on the electron side, ECs in $N = 1$ with reduced particle-hole pair excitation energy, have smaller gaps compared to the ECs in $N = 0$ with spin-texture excitations.

The evolution of the bulk resistance with D provides further insight into the identification of the two types of charged excitation. FIG. 3e plots the bulk resistance as a function of D for ECs at $\nu_{tot}=1$ and 5, corresponding to spin-texture and particle-hole excitation type respectively. The red curve regions around $D = 0$ mark EC regime and the system transition into integer quantum hall(IQH) phase(grey curve) with the increasing of D . Previous numerical study find that the excitation energy of meron-antimeron pairs show a sharp increase in gap with layer imbalance, while particle-hole excitation energy is independent of the layer imbalance until the zeeman energy exceeds the EC gap [35]. In our system, layer imbalance is regulated by D . In this scenario, we find a sharp $R_{xx-Bulk}$ decrease with D in red curve region for $\nu_{tot} = 1$ whereas at $\nu_{tot} = 5$, $R_{xx-Bulk}$ hold a mild response with D (Fig. 3e). This suggests that ECs on electron side in $N = 0$ LL host the spin-texture charged excitation while ECs in $N = 1$ LL have a particle-hole excitation(At $\nu_{tot}=1$ in $N = 0$ LL, red curve corresponding to meron-antimeron-type ECs with lager slope than gray curve corresponding to IQH, and At $\nu_{tot}=1$ in $N = 1$ LL, red curve corresponding to particle-hole-type ECs with smaller slope than gray curve corresponding to IQH.). On the other hand, on the hole side, ECs in both $N = 0$ and 1 exhibit sharp $R_{xx-Bulk}$ changes, corresponding a spin-texture charged excitation(FIG. S8). This result is consistent with our theoretical calculation that the low-energy charged excitation of ECs is different on electron and hole sides.

Finally, to fully identify the nature of ECs, we

demonstrate the evolution of ECs with magnetic field. FIG. 4a shows B dependence of $R_{xx-Bulk}$ for all the ECs at $D = 0$ V/nm. The $R_{xx-Bulk}$ of all ECs decreases with diminishing of B indicating that our system is in strong coupling regime. In this regime, the main effect of increasing the magnetic field is to raise the excitons density($\propto B$), rather than increasing the $d/l_B(\propto \sqrt{B})$ to soften the exciton pairing strength, which is preferred in weak coupling system [12]. We further find that all ECs gaps are positively correlated with magnetic field and well fit by $\Delta = E_c/E_c(14T)$ (red dashed line in FIG. 4b) which is in line with our numerical calculations (Supplementary Information section 5). Both of the particle-hole and the spin-texture excitation energies are related to stiffness ($\rho_s \sim 1/l_B$), causing the excitation energy is proportional to the Coulomb energy ($E_c = e^2/l_B$) (Supplementary Information section 5). Furthermore, it is worth noting that the $N = 1$ orbital in BLG differs from conventional $n = 1$ orbital. In BLG, $N = 1$ orbital contains a combination of both conventional LL orbital $n = 0$ and $n = 1$ wavefunctions distributed on different atomic sites of BLG, with the relative weight of $n = 0$ wavefunction increasing with B [31, 32]. Hence, under higher magnetic fields beyond our experiments (about $B > 25T$) [31, 32], the extensive participation of $n = 0$ wavefunction in BLG $N = 1$ orbital renders ECs in decoupled bilayers prone to hold excitation energy deviating from the trend of E_c .

In summary, we have experimentally observed remarkable magneto-excitons and their EC phase in ZLL region of large-angle twisted TDBG. Interlayer tunneling is suppressed by large momentum mismatch and we demonstrate the ECs in the strong coupling limit with sub-nanometer atomic separation between the two bilayers. The different carrier screening strengths in electron and hole sides lead to distinct stability of ECs in both carrier types and the evolution of ECs with LL index unveiled a change of the low-energy charged excitation from meron-antimeron pair to particle-hole pair on different carrier doping types. The variations in pairing behavior concerning magnetic field, doping, and temperature are summarized in FIG. 4c. Using electrostatic gating, thus we achieved unprecedentedly modulating the topology of low-energy charged excitation of ECs, providing further opportunities on application of skyrmion-type devices in magnetic data storage and topological quantum computing. Moreover, the signature of incompressible states in finite displacement field may lead to an unconventional route to explore non-equilibrium ECs[36] or multi-polar excitonic [37] physics.

-
- [1] J. M. Blatt, K. Böer, and W. Brandt, Bose-einstein condensation of excitons, *Physical Review* **126**, 1691 (1962).
- [2] D. Snoke, Spontaneous bose coherence of excitons and polaritons, *Science* **298**, 1368 (2002).
- [3] B. Halperin and T. Rice, Possible anomalies at a semimetal-semiconductor transistion, *Reviews of Modern Physics* **40**, 755 (1968).
- [4] W. Kohn and D. Sherrington, Two kinds of bosons and bose condensates, *Reviews of Modern Physics* **42**, 1 (1970).
- [5] E. Baldini, A. Zong, D. Choi, C. Lee, M. H. Michael, L. Windgatter, I. I. Mazin, S. Latini, D. Azoury, B. Lv, *et al.*, The spontaneous symmetry breaking in ta2nise5 is structural in nature, *Proceedings of the National Academy of Sciences* **120**, e2221688120 (2023).
- [6] J. Eisenstein and A. H. MacDonald, Bose-einstein condensation of excitons in bilayer electron systems, *Nature* **432**, 691 (2004).
- [7] J. Eisenstein, Exciton condensation in bilayer quantum hall systems, *Annu. Rev. Condens. Matter Phys.* **5**, 159 (2014).
- [8] D. Nandi, A. Finck, J. Eisenstein, L. Pfeiffer, and K. West, Exciton condensation and perfect coulomb drag, *Nature* **488**, 481 (2012).
- [9] M. Kellogg, I. Spielman, J. Eisenstein, L. Pfeiffer, and K. West, Observation of quantized hall drag in a strongly correlated bilayer electron system, *Physical review letters* **88**, 126804 (2002).
- [10] X. Liu, K. Watanabe, T. Taniguchi, B. I. Halperin, and P. Kim, Quantum hall drag of exciton condensate in graphene, *Nature Physics* **13**, 746 (2017).
- [11] J. Li, T. Taniguchi, K. Watanabe, J. Hone, and C. Dean, Excitonic superfluid phase in double bilayer graphene, *Nature Physics* **13**, 751 (2017).
- [12] X. Liu, J. I. A. Li, K. Watanabe, T. Taniguchi, J. Hone, B. I. Halperin, P. Kim, and C. R. Dean, Crossover between strongly coupled and weakly coupled exciton superfluids, *Science* **375**, 205 (2022).
- [13] Y. Zeng, Q. Shi, A. Okounkova, D. Sun, K. Watanabe, T. Taniguchi, J. Hone, C. R. Dean, and J. I. A. Li, Evidence for a superfluid-to-solid transition of bilayer excitons (2023), arXiv:2306.16995 [cond-mat.mes-hall].
- [14] Q. Shi, E.-M. Shih, D. Rhodes, B. Kim, K. Barmak, K. Watanabe, T. Taniguchi, Z. Papić, D. A. Abanin, J. Hone, *et al.*, Bilayer wse2 as a natural platform for interlayer exciton condensates in the strong coupling limit, *Nature Nanotechnology* **17**, 577 (2022).
- [15] P. Rickhaus, G. Zheng, J. L. Lado, Y. Lee, A. Kurzman, M. Eich, R. Pisoni, C. Tong, R. Garreis, C. Gold, M. Masseroni, T. Taniguchi, K. Watanabe, T. Ihn, and K. Ensslin, Gap opening in twisted double bilayer graphene by crystal fields, *Nano Letters* **19**, 8821 (2019).
- [16] S. Kim, D. Kim, K. Watanabe, T. Taniguchi, J. H. Smet, and Y. Kim, Orbitaly controlled quantum hall states in decoupled two-bilayer graphene sheets, *Advanced Science* , 2300574 (2023).
- [17] D. Kim, B. Kang, Y.-B. Choi, K. Watanabe, T. Taniguchi, G.-H. Lee, G. Y. Cho, and Y. Kim, Robust interlayer-coherent quantum hall states in twisted bilayer graphene, *Nano Letters* **23**, 163 (2022).
- [18] K. Moon, H. Mori, K. Yang, S. Girvin, A. MacDonald, L. Zheng, D. Yoshioka, and S.-C. Zhang, Spontaneous interlayer coherence in double-layer quantum hall systems: Charged vortices and kosterlitz-thouless phase transitions, *Physical Review B* **51**, 5138 (1995).
- [19] L. Wang, I. Meric, P. Y. Huang, Q. Gao, Y. Gao, H. Tran, T. Taniguchi, K. Watanabe, L. M. Campos, D. A. Muller, J. Guo, P. Kim, J. Hone, K. L. Shepard, and C. R. Dean, One-dimensional electrical contact to a two-dimensional material, *Science* **342**, 614 (2013).
- [20] R. Puddy, P. Scard, D. Tyndall, M. Connolly, C. Smith, G. Jones, A. Lombardo, A. Ferrari, and M. Buitelaar, Atomic force microscope nanolithography of graphene: cuts, pseudocuts, and tip current measurements, *Applied Physics Letters* **98** (2011).
- [21] P. Rickhaus, F. K. d. Vries, J. Zhu, E. Portoles, G. Zheng, M. Masseroni, A. Kurzman, T. Taniguchi, K. Watanabe, A. H. MacDonald, T. Ihn, and K. Ensslin, Correlated electron-hole state in twisted double-bilayer graphene, *Science* **373**, 1257 (2021).
- [22] F. K. de Vries, J. Zhu, E. Portolés, G. Zheng, M. Masseroni, A. Kurzman, T. Taniguchi, K. Watanabe, A. H. MacDonald, K. Ensslin, T. Ihn, and P. Rickhaus, Combined minivalley and layer control in twisted double bilayer graphene, *Phys. Rev. Lett.* **125**, 176801 (2020).
- [23] E. McCann and V. I. Fal'ko, Landau-level degeneracy and quantum hall effect in a graphite bilayer, *Phys. Rev. Lett.* **96**, 086805 (2006).
- [24] B. Sun, W. Zhao, T. Palomaki, Z. Fei, E. Runburg, P. Malinowski, X. Huang, J. Cenker, Y.-T. Cui, J.-H. Chu, *et al.*, Evidence for equilibrium exciton condensation in monolayer wte2, *Nature Physics* **18**, 94 (2022).
- [25] K. Muraki, T. Saku, and Y. Hirayama, Charge excitations in easy-axis and easy-plane quantum hall ferromagnets, *Physical review letters* **87**, 196801 (2001).
- [26] X. Zhang, I. Martin, and H. Jiang, Landau level anti-crossing manifestations in the phase-diagram topology of a two-subband system, *Physical Review B* **74**, 073301 (2006).
- [27] B. Hunt, J. Li, A. Zibrov, L. Wang, T. Taniguchi, K. Watanabe, J. Hone, C. Dean, M. Zaletel, R. Ashoori, *et al.*, Direct measurement of discrete valley and orbital quantum numbers in bilayer graphene, *Nature communications* **8**, 948 (2017).
- [28] V. W. Scarola, K. Park, and J. Jain, Cooper instability of composite fermions, *Nature* **406**, 863 (2000).
- [29] R. Willett, J. P. Eisenstein, H. L. Störmer, D. C. Tsui, A. C. Gossard, and J. English, Observation of an even-denominator quantum number in the fractional quantum hall effect, *Physical review letters* **59**, 1776 (1987).
- [30] W. Pan, J.-S. Xia, V. Shvarts, D. Adams, H. Stormer,

- D. Tsui, L. Pfeiffer, K. Baldwin, and K. West, Exact quantization of the even-denominator fractional quantum hall state at $\nu = 5/2$ Landau level filling factor, *Physical Review Letters* **83**, 3530 (1999).
- [31] A. A. Zibrov, C. Kometter, H. Zhou, E. Span-ton, T. Taniguchi, K. Watanabe, M. Zaletel, and A. Young, Tunable interacting composite fermion phases in a half-filled bilayer-graphene Landau level, *Nature* **549**, 360 (2017).
- [32] J. Li, C. Tan, S. Chen, Y. Zeng, T. Taniguchi, K. Watanabe, J. Hone, and C. Dean, Even-denominator fractional quantum hall states in bilayer graphene, *Science* **358**, 648 (2017).
- [33] S. Girvin and A. MacDonald, Multicomponent quantum hall systems: The sum of their parts and more, *Perspectives in Quantum Hall Effects: Novel Quantum Liquids in Low-Dimensional Semiconductor Structures*, 161 (1996).
- [34] X.-G. Wu and S. Sondhi, Skyrmions in higher Landau levels, *Physical Review B* **51**, 14725 (1995).
- [35] V. Bayot, E. Grivei, J.-M. Beuken, S. Melinte, and M. Shayegan, Critical behavior of nuclear-spin diffusion in GaAs/AlGaAs heterostructures near Landau level filling $\nu = 1$, *Physical Review Letters* **79**, 1718 (1997).
- [36] B. Zou, Y. Zeng, A. MacDonald, and A. Strashko, Electrical control of two-dimensional electron-hole fluids in the quantum hall regime, *arXiv preprint arXiv:2309.04600* (2023).
- [37] D. D. Dai and L. Fu, Strong-coupling phases of trions and excitons in electron-hole bilayers at commensurate densities, *arXiv preprint arXiv:2308.00825* (2023).
- [38] D. Pfannkuche and R. R. Gerhardts, Theory of magnetotransport in two-dimensional electron systems subjected to weak two-dimensional superlattice potentials, *Phys. Rev. B* **46**, 12606 (1992).
- [39] J. A. Crosse, N. Nakatsuji, M. Koshino, and P. Moon, Hofstadter butterfly and the quantum hall effect in twisted double bilayer graphene, *Phys. Rev. B* **102**, 035421 (2020).
- [40] Z. Ezawa and Z. Ezawa, *Quantum Hall Effects: Field Theoretical Approach and Related Topics* (World Scientific, 2000).
- [41] K. Moon, H. Mori, K. Yang, S. M. Girvin, A. H. MacDonald, L. Zheng, D. Yoshioka, and S.-C. Zhang, Spontaneous interlayer coherence in double-layer quantum hall systems: Charged vortices and Kosterlitz-Thouless phase transitions, *Phys. Rev. B* **51**, 5138 (1995).
- [42] K. Yang, S. Das Sarma, and A. H. MacDonald, Collective modes and skyrmion excitations in graphene $su(4)$ quantum hall ferromagnets, *Phys. Rev. B* **74**, 075423 (2006).
- [43] D. P. Arovas, A. Karlhede, and D. Lilliehöök, $SU(n)$ quantum hall skyrmions, *Phys. Rev. B* **59**, 13147 (1999).

ACKNOWLEDGMENTS

L.W. acknowledges the National Key Projects for Research and Development of China (Grant

Nos. 2022YFA120470, 2021YFA1400400), National Natural Science Foundation of China (Grant No. 12074173) and Program for Innovative Talents and Entrepreneur in Jiangsu (Grant No. JSSCTD202101). K.W. and T.T. acknowledge support from the JSPS KAKENHI (Grant Numbers 20H00354 and 23H02052) and A3 Foresight by JSPS. K.S.N. is grateful to the Ministry of Education, Singapore (Research Centre of Excellence award to the Institute for Functional Intelligent Materials, I-FIM, project No. EDUNC-33-18-279-V12) and to the Royal Society (UK, grant number RSRP R 190000) for support.

AUTHOR CONTRIBUTIONS

L.W., Q.L. conceived the experiment. Q.L., Y.C., L.N.W., H.Y. fabricated the samples. Q.L., Y.C., L.W. performed transport measurement and data analysis. R.W., H.C. performed theoretical calculations. K.W. and T.T. supplied hBN crystals. Q.L., Y.C., H.C. and L.W. wrote the manuscript with input from all co-authors.

COMPETING INTEREST DECLARATION

The authors declare no competing interest.

DATA AVAILABILITY

The data that support the findings of this study are available from the corresponding authors upon request.

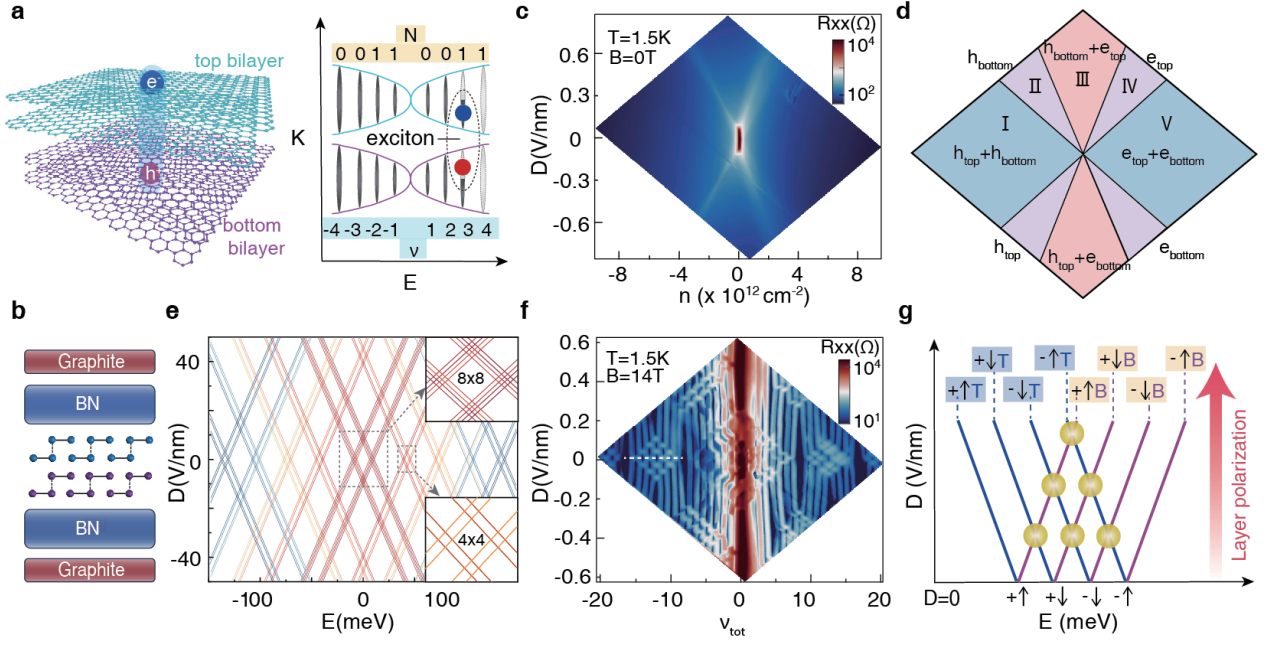


FIG. 1. Large-angle TDBG Landau level structure and decoupled carrier population. **a**, Illustration of magneto-excitons in TDBG. The interlayer tunneling is suppressed by large momentum mismatch, and at finite magnetic field, strong interaction induces electron-like carriers in a half-filled LL in one layer coupling with hole-like carriers in the other, forming interlayer magneto-excitons. **b**, Schematic of the TDBG device structure. **c-d**, Longitudinal resistance R_{xx} of TDBG at $B = 0$ T and $T = 1.5$ K, versus n and D . The map exhibits the different population of charge carriers in two bilayers and the ‘layer-targeted’ population divides the diagram into different regions highlighted in (d). **e**, Calculated LL spectra as a function of energy E and D at $B = 14$ T. Inset: Zooming-in on the LL crossings in the 8×8 matrix (top) (accidental degeneracy for $N = 0$ and 1) and a typical 4×4 (bottom) matrix (for $N \geq 2$), respectively. **f**, Longitudinal resistance R_{xx} of TDBG at $B = 14$ T and $T = 1.5$ K, versus ν_{tot} and D . White dashed line marks the four QHSs stabilized by the spin and valley degeneracy lifting at $D = 0$ V/nm in non-zero LL. **g**, Schematic illustration of LL crossings driven by displacement field under a constant magnetic field. ‘T’: top bilayer; ‘B’: bottom bilayer.

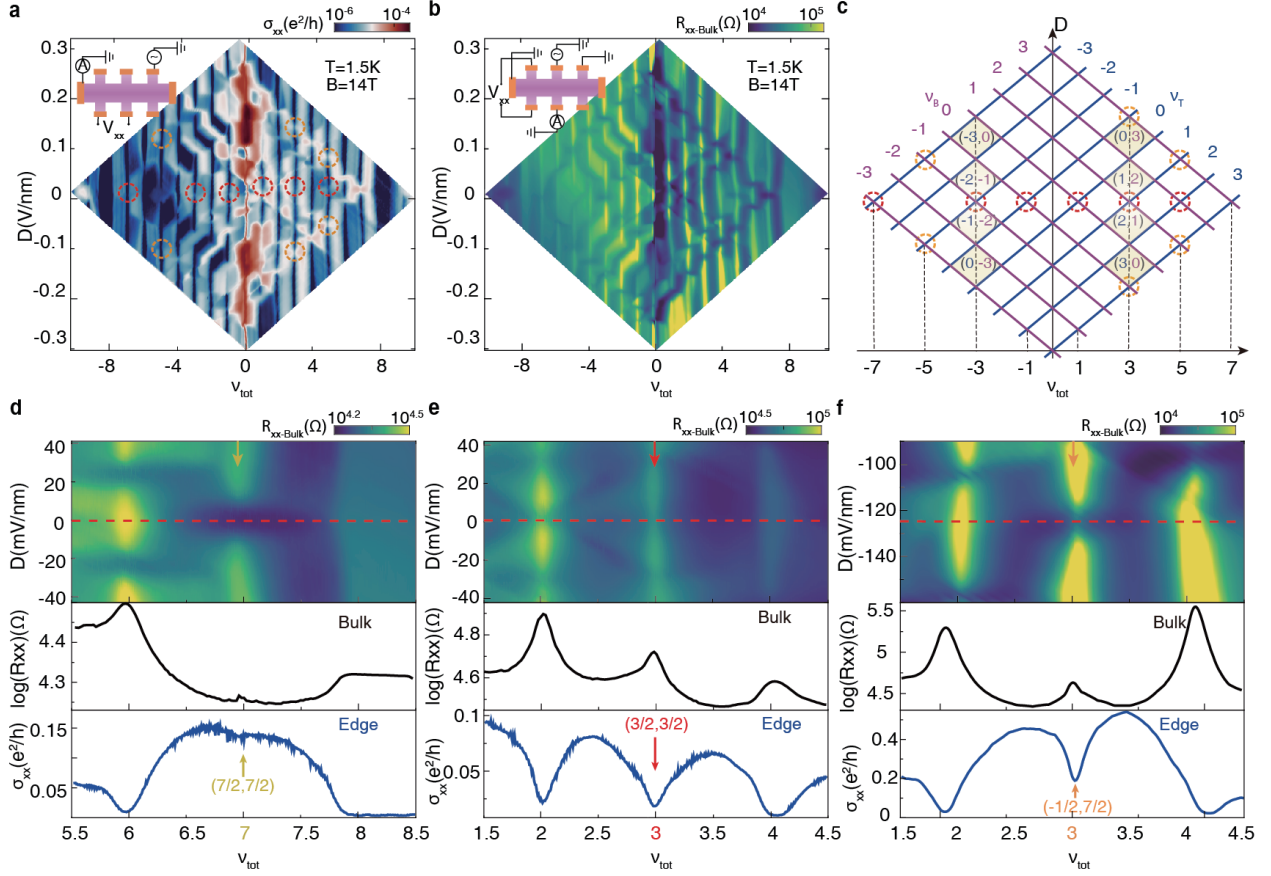


FIG. 2. **ECs in the zero-energy Landau level matrix.** **a-b**, The longitudinal conductance σ_{xx} (a) and bulk resistance $R_{xx-Bulk}$ (b) versus D and ν_{tot} at $B = 14$ T and $T = 1.5$ K for $-9 < \nu_{tot} < 9$. Dotted red circles (a) and orange circles mark the LL crossings manifesting as anomalous conductivity minimum states at $D = 0$ and $D \neq 0$, respectively. The insets show the measurement configurations. To measure $R_{xx-Bulk}$, two contacts are grounded to make sure the signal comes from the bulk instead of edge resistance of the sample. **c**, Schematic LL diagram for $-8 < \nu_{tot} < 8$. These LL crossings originate from the cross of zero-energy LLs octet of two decoupled bilayers which are marked by different colours. Yellow shades mark two typical IQH regions with the filling factor marked as (ν_T, ν_B) . **d-f**, Top panel displays enlarge images of $R_{xx-Bulk}$ versus ν_{tot} and D at $B = 14$ T around the three categories LL crossings illustrated in maintext. In each bottom panel, the black curve is the bulk resistance linecut along the red dashed line in the top panel, while the blue curve is the longitudinal conductance linecut in (a). The yellow, red, and orange arrows point to normal LL crossings, ECs, and less-developed ECs, respectively.

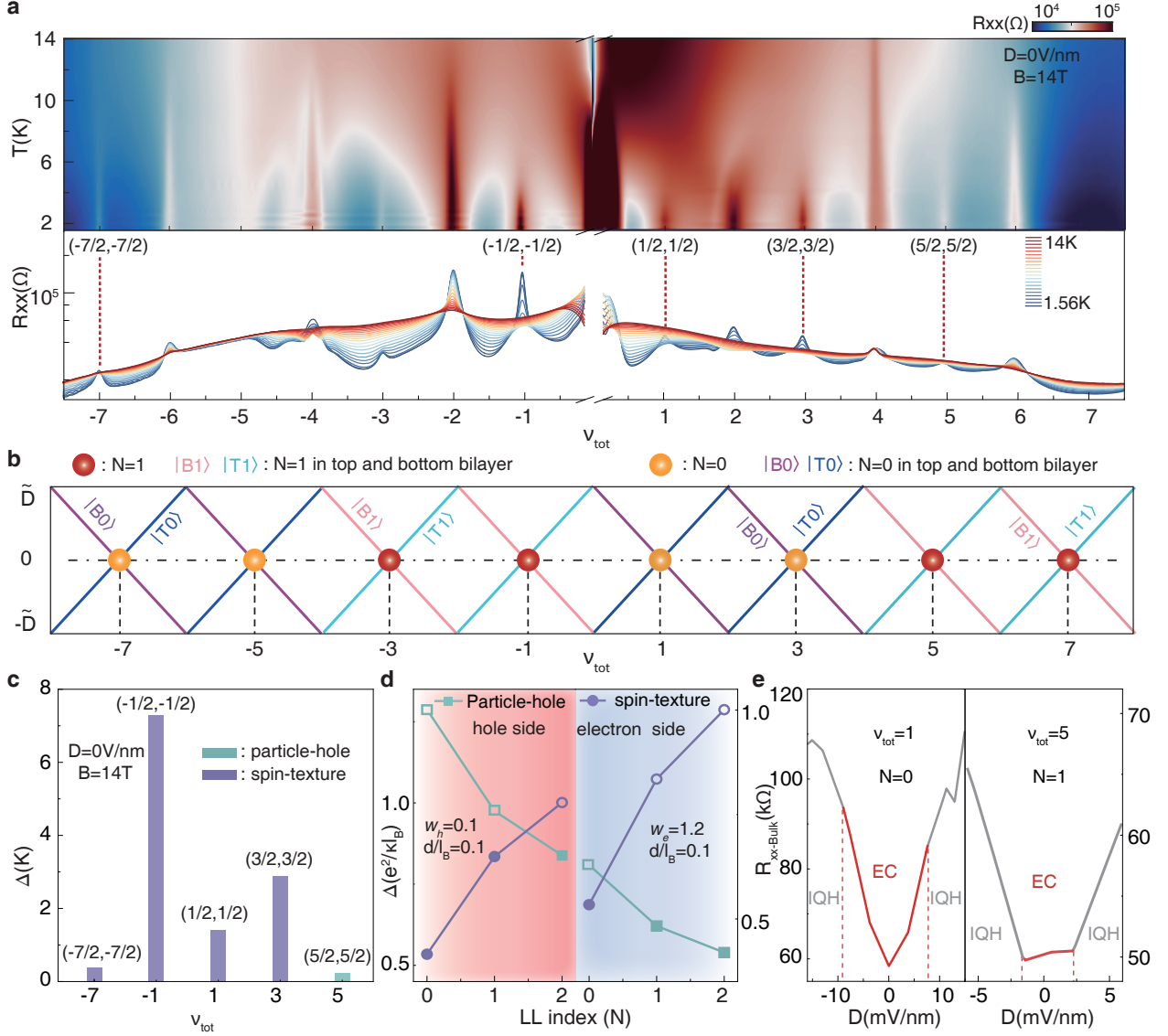


FIG. 3. Energy gap of ECs and the low-energy charged excitations. **a**, Temperature dependence of $R_{xx-Bulk}$ as a function of ν_{tot} at $D = 0$ V/nm and $B = 14$ T. Red dotted lines mark the ECs corresponding to both bilayers are half-filled. **b**, Evolution of orbital occupancy ($N = 0, N = 1$) with total filling factors in decoupled TDBG. **c**, Excitation energy gaps of ECs at $B = 14$ T and $D = 0$ V/nm. Purple rectangles correspond to ECs with the spin-texture charged excitation and green rectangle corresponds to EC with the particle-hole charged excitation. **d**, Theoretical calculations of energy gap for two types of excitations on hole and electron sides, at $d/l_B = 0.1$ and $D = 0$ V/nm. Owing to the distinct electron and hole environments, we use the parameter ' w ' to quantify the strength of screening effects. Since the screening effect of carriers is weak when filling the zero-energy Landau level starting from hole side, we take $w_h = 0.1$. Conversely, the screening effect is already significant when carriers fill the electron side, so we take the average screening effect for electron side as $w_e = 1.2$. The spin-texture excitation energy increases with LL index while particle-hole excitation energy decreases with LL index. Their crossing points for hole and electron sides appear at different positions of LL index due to the screening strength increasing with total filling. The filled markers represent the low-energy excitations of ECs. **e**, $R_{xx-Bulk}$ as a function of D for the ECs at $\nu_{tot} = 1, 5$, which correspond to $N = 0$ and 1 LL, respectively. Red curve regions mark ECs and grey curves correspond to IQH regime. At $\nu_{tot} = 1$ in $N = 0$ LL, red curve corresponding to meron-antimeron-type ECs with larger slope than grey curve corresponding to IQH, and At $\nu_{tot} = 1$ in $N = 1$ LL, red curve corresponding to particle-hole-type ECs with smaller slope than grey curve corresponding to IQH. (The rate of change of the bulk resistance with the displacement field near $D = 0$ (the magnitude of the slope) determines the phase boundaries of different phases.)

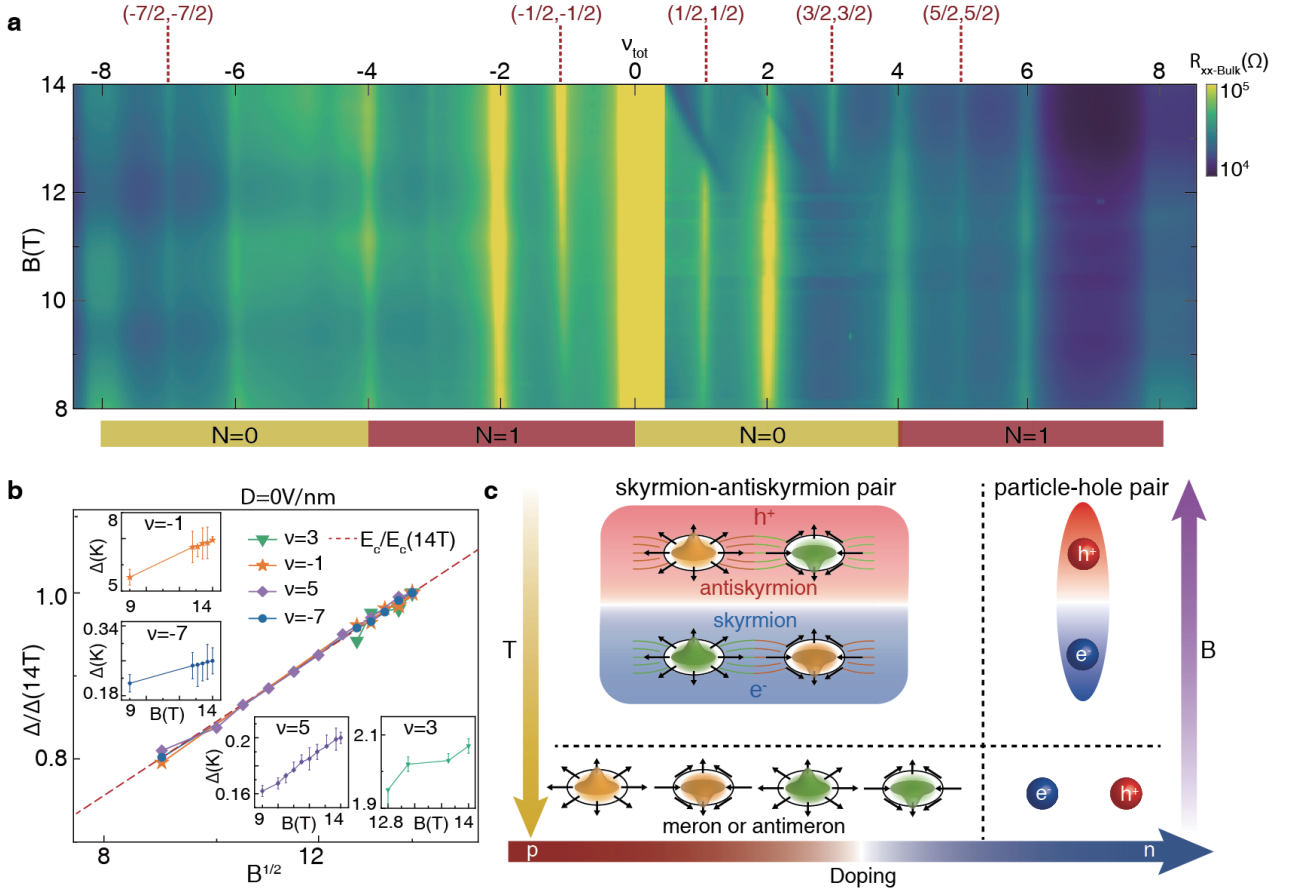


FIG. 4. **Evolution of ECs with magnetic field.** **a**, The $R_{xx-Bulk}$ versus B and ν_{tot} at $D = 0$ V/nm and $T = 1.55$ K for $-9 < \nu_{tot} < 9$. **b**, Scaled activation gap $\Delta/\Delta(14T)$ of ECs at different total fillings as a function of \sqrt{B} for $9T \leq B \leq 14$ T. The red dashed curve corresponds to the scaled Coulomb energy, $E_c/E_c(14T) (\propto \sqrt{B})$. Insets: details of activation gaps of each EC at different magnetic fields. **c**, Illustration of the low-energy charged excitations of ECs and their evolution with tuning temperature(T), magnetic field(B) and carrier density. The bottom panel shows four types of merons(antimerons) (left) and free electrons and holes(right). A meron and an antimeron have opposite vorticity, but carry the same electric charge($\pm e/2$) and they can pair to form skyrmion or antiskyrmion which both carry unit of topological charge($\pm e$) but with opposite charge.(shown in top left panel). The spin-texture(particle-hole) EC ground states form by pairing skyrmions and anti-skyrmions (electrons and holes) at low temperature and finite magnetic field. Increasing doping would make the low-energy charged excitation of ECs change from spin-texture type to particle-hole type.

Supplementary Information for
**Strongly coupled magneto-excitons in large-angle twisted double
bilayer graphene**

Qingxin Li *et al.*

Corresponding authors: Rui Wang, ruiwang@nju.edu.cn; Geliang Yu, yugeliang@nju.edu.cn;
Lei Wang, leiwang@nju.edu.cn

1. SAMPLE FABRICATION AND MEASUREMENT SETUP

The three devices (device A~C) in our text were all fabricated using the ‘cut-and-stack’ technique[19]. The raw materials for the preparation of each device, hexagonal boron nitride(hBN)(about 30nm), graphite and bilayer graphene are obtained from mechanically exfoliation onto Si/SiO_2 substrate. Their thickness and quality were then identified by optical microscopy and atomic force microscopy. Before stacking, we first cut the bilayer graphene into two pieces using atomic force microscopy. Then we used hBN, grphite and pre-cut bilayer graphene pieces to assembled the graphite/BN/tDBG/BN/grphite stack using dry pick-up technique with a stamp consisting of polypropylene carbonate(PPC) film and polydimethylsiloxane(PDMS). Using graphite as the gate above and below the TDBG reduces the disorder and defects introduced during evaporation compared to metal gates. The stack is then annealed under high vacuum at $400^\circ C$ for 15 minutes. Next we defined the geometry of the topgate and hall bar by CHF_3/O_2 etching. Finally, electrode contact was evaporated with Cr/Pd/Au (5/15/100nm) metal by e-beam evaporation.

Transport measurements were carried out in cryogenic superconducting magnets with base temperature of 1.5K. The four-terminal resistance were measured using low-frequency lock-in techniques at 17.777Hz with a current excitation of $20nA$.

2. DECOUPLED BEHAVIOR AT FINITE MAGNETIC FIELD.

Here, we analyze the Shubnikov–de Haas (SdH) oscillations at finite magnetic field. FIG. S2a shows the plot of longitudinal resistance $\log(R_{xx})$ versus the D and carrier density n at $B=4T$. Noticeable decoupled behavior, with the same driving mechanism at zero field, is conformed by evolution of different regions(separated by the black dashed lines) in phase diagram. For further analyzing decoupled behavior at finite magnetic field, we present the fan diagram $\log(R_{xx})(n, B)$ at $D=1.25V/nm$ (marked as red dashed line in FIG. S2a) as shown in FIG. S2b. There are five qualitatively different regions at different n range, which correspond to the different charge carriers occupation in TDBG, which can be interpreted by single-particle band structure shown in FIG. S2c-g. In large carrier density like region I and V, both bilayers (top and bottom) are prone to be populated by holes and electrons respectively, illustrated in FIG. S2c and g; Reducing carrier density n to region II or IV, only one piece of bilayer(top or bottom) is populated while the other bilayer’s fermi energy is in the band gap, illustrated in FIG. S2d and f; Finally, in the vicinity of CNP(region III), both bilayers are populated by co-existing hole and electron charge carriers illustrated in FIG. S2e. The overlapping electron-hole bands are mark by crossing of red line and blue line, which are on behalf of electron bands and holes bands,respectively.

3. LANDAU LEVELS CROSSING STRUCTURE

We here explore the Landau levels crossing structures in the decoupled TDBG model. Taking the spin and valley into consideration, the $N = 0, 1$ Landau levels for τ bilayer, where $\tau = \pm 1$ for the top or bottom bilayer respectively, in the valley ξ are

$$\begin{aligned} E_0 &= \frac{1}{2}\xi u \pm E_Z/2 + \tau D/2 \\ E_1 &= \xi \left(\frac{1}{2}u - \delta \right) \pm E_Z/2 + \tau D/2 \end{aligned} \quad (S1)$$

where $\delta = u\hbar\omega_c/\gamma_1$ reflects the valley splitting, and the two layers are distinguished by the on-site energies $\pm \frac{u}{2}$ [23]. D denotes the displacement field. For the higher Landau levels, i.e., $N > 1$, the Landau levels read as

$$E_N^\pm = \pm \hbar\omega_c \sqrt{N(N-1)} - \frac{1}{2}\xi\delta \pm E_Z/2 + \tau D/2 \quad (S2)$$

When the displacement field varies, the Landau levels of two bilayers tilt in opposite directions, resulting in a crossing of Landau Levels. The lowest two Landau levels i.e. $N = 0, 1$, interlace to form an 8x8 crossing structure shown in maintext Fig. 1e.

4. NUMERICAL ESTIMATION OF THE TUNNELING GAP

There are two possible origins for the gap formed between the electron and hole Landau levels in the TDBG. One is the excitonic gap due to the correlation effect, and the other is the hybridization gap due to the electron tunneling between the two bilayers. The second mechanism can be excluded for the case with large twisted angle around 10° . This can be achieved by examining the tunneling strength, i.e., the off-diagonal elements connecting different bilayers of the TDBG Hamiltonian under magnetic fields.

In the Landau gauge, the eigenstate $|N, k_y\rangle$ reads as

$$\psi_{Nk_y}(x, y) = L_y^{-1/2} \exp(ik_y y) \phi_N(x - l_B^2 k_y), \quad (\text{S3})$$

with n denoting the LL index. At zero magnetic field, the TDBG system (valley + or -) can be described by a continuum model:

$$H = \sum_{\mathbf{k}} \Psi_{\alpha}^{\dagger}(\mathbf{k}) h_{\alpha,\beta}(\mathbf{k}) \Psi_{\beta}(\mathbf{k}) + \sum_{\mathbf{k}, \mathbf{Q}_j} \Psi_{\alpha}^{\dagger}(\mathbf{k}) T_{\alpha,\beta}(\mathbf{Q}_j) \Psi_{\beta}(\mathbf{k}) \quad (\text{S4})$$

where α, β are the combination of layer and sublattice indices. The second term of Eq.(S4) describes the moiré hopping from momentum \mathbf{k} (relative to the Dirac point) to momentum $\mathbf{k} + \mathbf{Q}_j$, where $\mathbf{Q}_1 = (0, \frac{4\pi}{3a_M})$, $\mathbf{Q}_2 = (-\frac{2\pi}{\sqrt{3}a_M}, -\frac{2\pi}{3a_M})$ and $\mathbf{Q}_3 = (\frac{2\pi}{\sqrt{3}a_M}, -\frac{2\pi}{3a_M})$. The TDBG under magnetic fields is then described by the Landau quantization of Hamiltonian(S4). From Eq.(S3) and Eq.(S4), we can read off the off-diagonal matrix elements describing the tunneling between the Landau states from different bilayers, i.e.,

$$\begin{aligned} U_{N'k'_y, Nk_y} &= w \langle N'k'_y | \exp(i\mathbf{Q} \cdot \mathbf{r}) | N, k_y \rangle \\ &= w \delta_{k'_y, k_y + Q_y} \sqrt{\frac{\lambda!}{\Lambda!}} \left(\frac{Q_x + iQ_y}{|\mathbf{Q}|} \right)^{N-N'} \left(\frac{i|\mathbf{Q}|l_B}{\sqrt{2}} \right)^{|N-N'|} \\ &\quad \times \exp\left(-\frac{|\mathbf{Q}|^2 l_B^2}{4} - \frac{i}{2} l_B^2 Q_x (k'_y + k_y)\right) L_{\lambda}^{|N-N'|} \left(\frac{|\mathbf{Q}|^2 l_B^2}{2} \right) \end{aligned} \quad (\text{S5})$$

where λ and Λ denote the cutoff of the Landau level indices N and N' , respectively, and L_{λ}^N is the associated Laguerre polynomial [38, 39].

One observes from Eq.(S5) an exponential factor $\exp(-|\mathbf{Q}|^2 l_B^2)$, where $|\mathbf{Q}|$ is given by $4\pi/(3a_M)$ and $a_M = a/(2\sin(\theta/2))$ is the moiré lattice constant. For large twisted angle $\theta \sim 10^\circ$, $|\mathbf{Q}|$ is large and the tunneling strength is exponentially suppressed. We take the experimental parameters, i.e., $w = 110\text{meV}$, $\theta \sim 10^\circ$, $B = 14\text{T}$, and $a = 0.246\text{nm}$. Then the hybridization gap, which is of the same order of the tunneling strength, is obtained as $\Delta \sim U \sim 10^{-10}\text{meV}$. This is negligible, and is much smaller than the experimentally observed gap Δ_{ex} . Since $\Delta \sim U \sim 10^{-10}\text{meV} \ll \Delta_{ex}$, the interbilayer tunneling can be safely discarded when analyzing the correlation effect, which is dominant and becomes more manifested in the Landau levels physics under magnetic fields.

5. CALCULATION OF THE EXCITATION GAP

To calculate the excitation gap, according to the results in the last section, we discard the negligible tunneling gap and consider two graphene bilayers interacting with each other. The two bilayers are further subjected to a perpendicular magnetic field, thus exhibit Landau quantization characterized by the Landau index N_1, N_2 respectively. The excitonic gap is only favored in the balanced case where the electron and hole densities are equal, thus we focus on the case $N_1 = N_2 = N$, i.e., the electron and hole states are filled to the same Landau level. This leads to a twofold pseudospin degeneracy of the studied system.

The kinetic energy is completely suppressed under strong magnetic fields with well formed Landau levels. We thus need to project the Coulomb interaction onto the Landau levels. The interactions before projection reads as,

$$H_C = \frac{1}{2} \int d^2\mathbf{x} d^2\mathbf{y} V_{\alpha,\beta}(\mathbf{x} - \mathbf{y}) [\rho_{\alpha}(\mathbf{x}) - \rho_{\alpha,0}] [\rho_{\beta}(\mathbf{y}) - \rho_{\beta,0}], \quad (\text{S6})$$

where $\rho_{\alpha,0}$ is the average electron density which is determined by $\rho_{\alpha,0} = \nu_{\alpha}/2\pi l_B^2$, and the indices α, β are the pseudospin indices denoting the two bilayers. $V_{\alpha,\beta}(\mathbf{x})$ is the Coulomb potential and it has the following

Fourier components

$$V_{tt}(\mathbf{q}) = V_{bb}(\mathbf{q}) = \frac{2\pi}{|\mathbf{q}|}, \quad (\text{S7})$$

$$V_{tb}(\mathbf{q}) = V_{bt}(\mathbf{q}) = \frac{2\pi}{|\mathbf{q}|} e^{-d|\mathbf{q}|}, \quad (\text{S8})$$

where d is the spacing between the two bilayers which is set to $d/l_B = 0.1$ according to the experiments. The layer spacing within each bilayer is insignificant compared to d and is neglected here. The next step is to project Eq.(S6) onto the subspace of each Landau level, which leads to

$$V_N^{\alpha,\beta}(\mathbf{q}) = V_{\alpha,\beta}(\mathbf{q}) F_N^2(q) \quad (\text{S9})$$

where $F_N(\mathbf{q}) = L_n(l_B^2 q^2/2) \exp(-l_B^2 q^2/4)$ is the Landau level form factor, and $L_N(x)$ is an Laguerre polynomial [40].

In the absence of a displacement field, the top and bottom bilayers are symmetric in terms of their band structures. Under magnetic fields, and electron and hole Landau level can exhibits the same energy, leading to the crossing point as shown by Fig.2c of the main text. Interestingly, the correlation effect can lift the degeneracy of the LLs at the crossing points. For example, the attractive Coulomb force between an electron and a hole then would favor formation of excitons, leading to excitonic gap after condensation. Besides, the effect of the intra-bilayer interaction V_{tt} and V_{bb} also need to be carefully analyzed.

To analyze the correlation physics at the LL crossing points, we evaluate the excitation gaps with fully taking into account the interactions among the LLs. To this end, it is more convenient to introduce the Landau site basis [40], in which the Hamiltonian in Eq.(S6) is cast into:

$$H_C = \sum_{mnij} V_{mnij}^{\alpha,\beta} [\rho(n, m)^\alpha - \nu^\alpha \delta_{m,n}] [\rho(j, i)^\beta - \nu^\beta \delta_{i,j}], \quad (\text{S10})$$

and

$$V_{mnij}^{\alpha,\beta} = \frac{1}{4\pi} \int d^2\mathbf{k} V_N^{\alpha,\beta}(\mathbf{k}) \langle m | e^{i\mathbf{X}\mathbf{k}} | n \rangle \langle i | e^{-i\mathbf{X}\mathbf{k}} | j \rangle, \quad (\text{S11})$$

where $V_N^{\alpha,\beta}(\mathbf{k})$ is the projected coulomb interaction which is dependent on LLs, and $\rho^\alpha(n, m)$ is the Landau site density operator, where n, m denotes the degenerate states within each Landau level N .

We firstly calculate the energy cost to excite a particle-hole pair on top of the filled Landau state. For $N_1 = N_2 = N$, both bilayers have the $N > 0$ LLs occupied, and we assume that Landau levels $0, 1, 2, \dots, N-1$ are completely filled. Then, one considers the electron-hole pair state given by

$$|e_k; h_l\rangle = c_t^\dagger(k) c_b(l) |g\rangle, \quad (\text{S12})$$

where the ground state has the form $|g\rangle = \Pi_n c_b^\dagger(n) |0\rangle$, and $|0\rangle$ denotes the vacuum state. The excitation gap corresponding to the particle-hole excitation is then evaluated via

$$\begin{aligned} \Delta E &= \langle e_k; h_l | H_C | e_k; h_l \rangle - \langle g | H_C | g \rangle \\ &\approx \frac{1}{4\pi} \int d^2\mathbf{k} (V_{tt}(k) + V_{bb}(k)) \left[L_N\left(\frac{l_B^2 k^2}{2}\right) \right]^2 e^{-\frac{l_B^2 k^2}{2}}. \end{aligned} \quad (\text{S13})$$

This result is clearly LL dependent. The dependence of gap on the field B is then obtained as $\Delta E(B) \sim 1/l_B \sim \sqrt{B}$, as a direct result of the Landau form factor.

Certainly, it's crucial to recognize that, owing to the distinct electron and hole environments, their interactions differ when dealing with charged excitations. In this situation, electrons experience stronger screening than holes. We use the parameter ' w ' to quantify the strength of screening effects. We model the electron side Coulomb interaction as $2\pi e^{-w_e q l_B}/|\mathbf{q}|$, while the hole side potential is $2\pi e^{-w_h q l_B}/|\mathbf{q}|$, here the parameter w_e and w_h quantify the strength of screening effects of electron and hole sides. Since the screening effect of carriers is weak when filling the zero-energy Landau level starting from hole side, we take $w_h = 0.1$. Conversely, the screening effect is already significant when carriers fill the electron side, so we take the average screening effect for electron side as $w_e = 1.2$. Hence, similar to the calculation of Eq.(S13), taking into account the variation

in screening parameter, our calculations reveal that the energy of particle-hole type low-energy excitation on the electron side is lower than that on the hole side (shown in the FIG. S9)

In addition to particle-hole excitations, there is another typical charged excitations, i.e., the skyrmion and anti-skyrmion excitations. Treating the bilayer degrees of freedom as pseudospins, the excitations can carry nontrivial pseudospin textures. In our system where $d/l_B \neq 0$, the \hat{z} component of the order parameter is massive and the system has U(1) symmetry. In this scenario, topologically stable charged objects called meron and antimeron form, which have opposite vorticity, but carry the same topological charge($\pm e/2$) and can pair to skyrmion or antiskyrmion which both carry unit of topological charge($\pm e$) but with opposite charge. The skyrmion or anti-skyrmion configuration in the pseudospin textures are energetically favorable[41], which should be compared in energetics with the electron-hole excitations. Such pseudospin structures bear topological nontrivial properties, which was investigated in the context of $SU(M)$ quantum Hall ferromagnets. The minimum excitation energy for a Skyrmion pair is $\Delta_{SK} = 8\pi\rho_s$ [42, 43], where

$$\rho_s = \frac{1}{32\pi^2} \int_0^\infty q^3 V_N^{eff}(q) dq \quad (\text{S14})$$

denotes the stiffness of the order parameter and V_N^{eff} is the projected Coulomb potential[42, 43]. As discussed above, the tunneling between the two bilayers is negligible for $\theta \sim 10^\circ$, and thus the TDBG can be treated as an untwisted double bilayers when calculating the skyrmion pair excitation energy. In this scenario, the effective model here is described by the $SU(M) \times SU(M)$ quantum Hall ferromagnets with $M = 4$. Importantly, one observes that the stiffness in Eq.(S14) is independent of M . Thus, from Eq.(S14), the skyrmion pair excitation energy Δ_{SK} is obtained as $\Delta_{SK} \sim e^2/l_B \sim \sqrt{B}$, where l_B is the magnetic length.

Both of the particle-hole and the spin-texture excitation energies are related to stiffness ($\rho_s \sim 1/l_B$), consequently, the excitation energy is proportional to the Coulomb energy ($E_c = e^2/l_B$). We show the comparison between two types excitation gap as a function of the LL index n on both of hole and electron sides leads to FIG. S9(Fig. 3d of the main text).

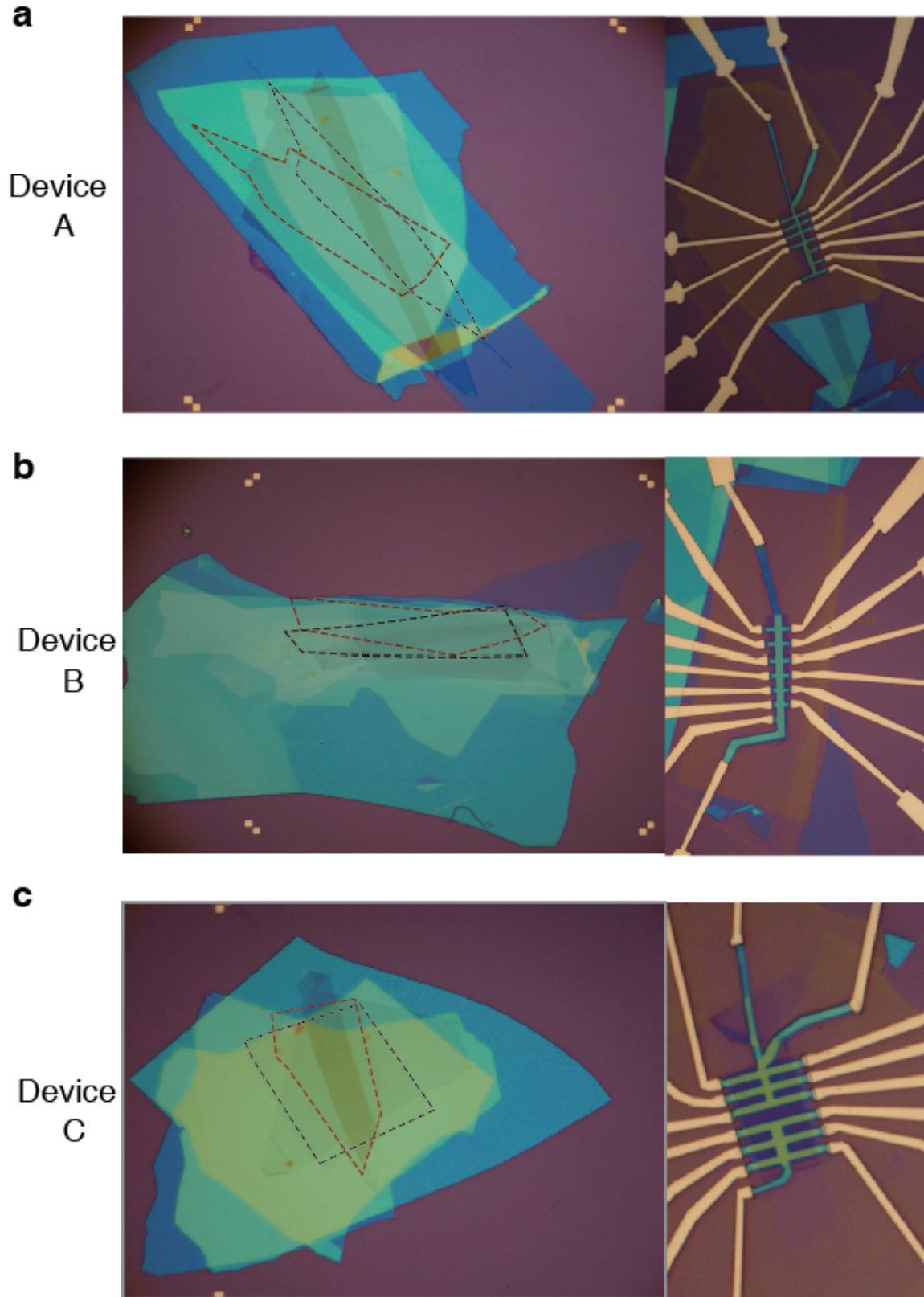


FIG. S1. Optical image of device. Optical image of three TDBG devices near 10° in the text. The dashed red and black lines denote two bilayer graphene sheets.

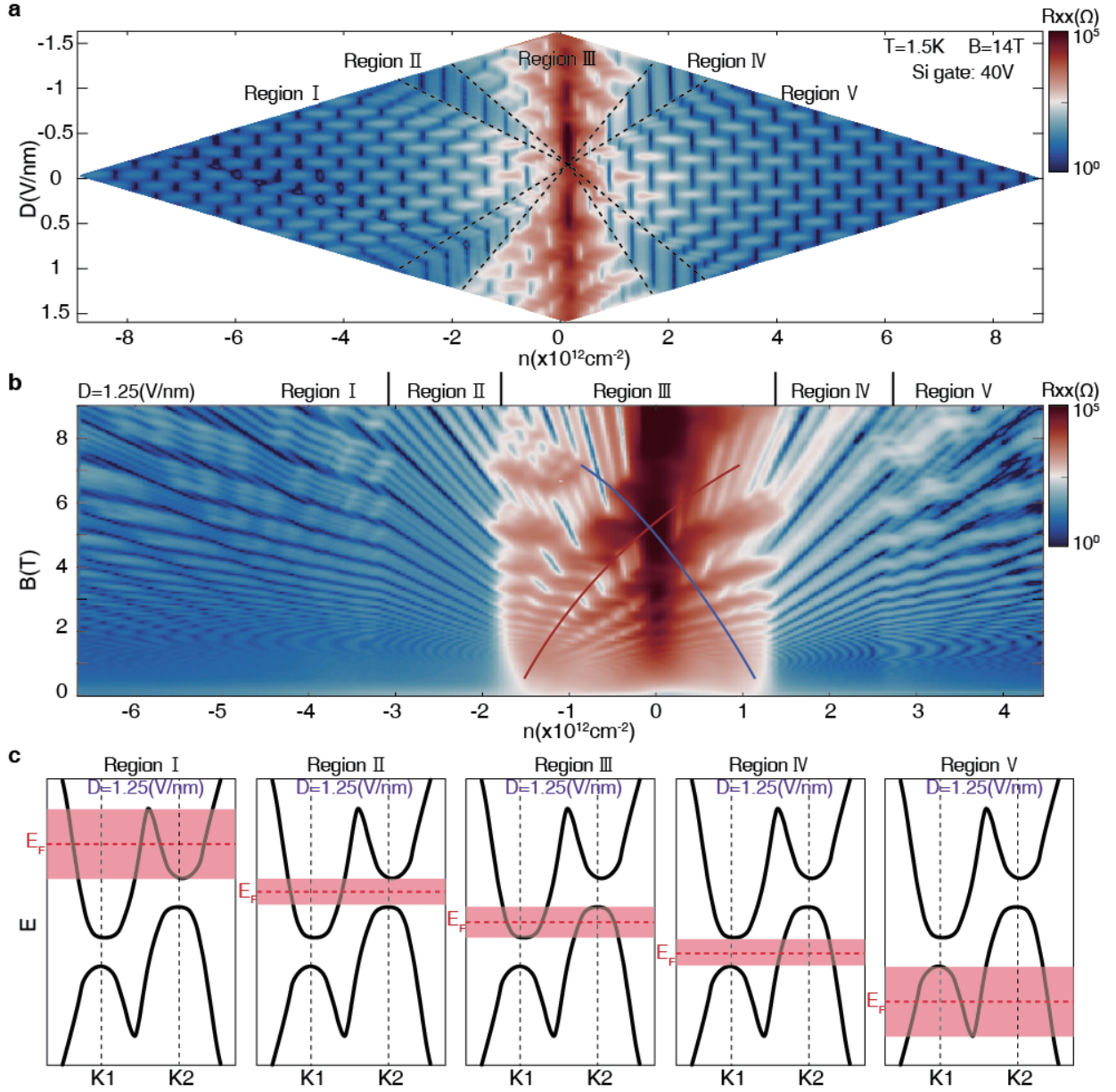


FIG. S2. Decoupled behavior at finite magnetic field. **a**, Longitudinal resistance R_{xx} of TDBG at $B=4\text{T}$ and $T=1.5\text{K}$, versus n and D . Black lines separate different regions which correspond to different charge carriers polarization in two bilayers. **b**, Longitudinal resistance R_{xx} versus B and n at $D=1.25\text{V/nm}$ and $T=1.5\text{K}$. Red and black lines in region III marked electron bands and holes bands, respectively. **c**, Schematic of the band structure near K point. $K1$ and $K2$ represent the K point of bottom and top bilayer, respectively. Red shaded areas represent the energy range of corresponding regions.

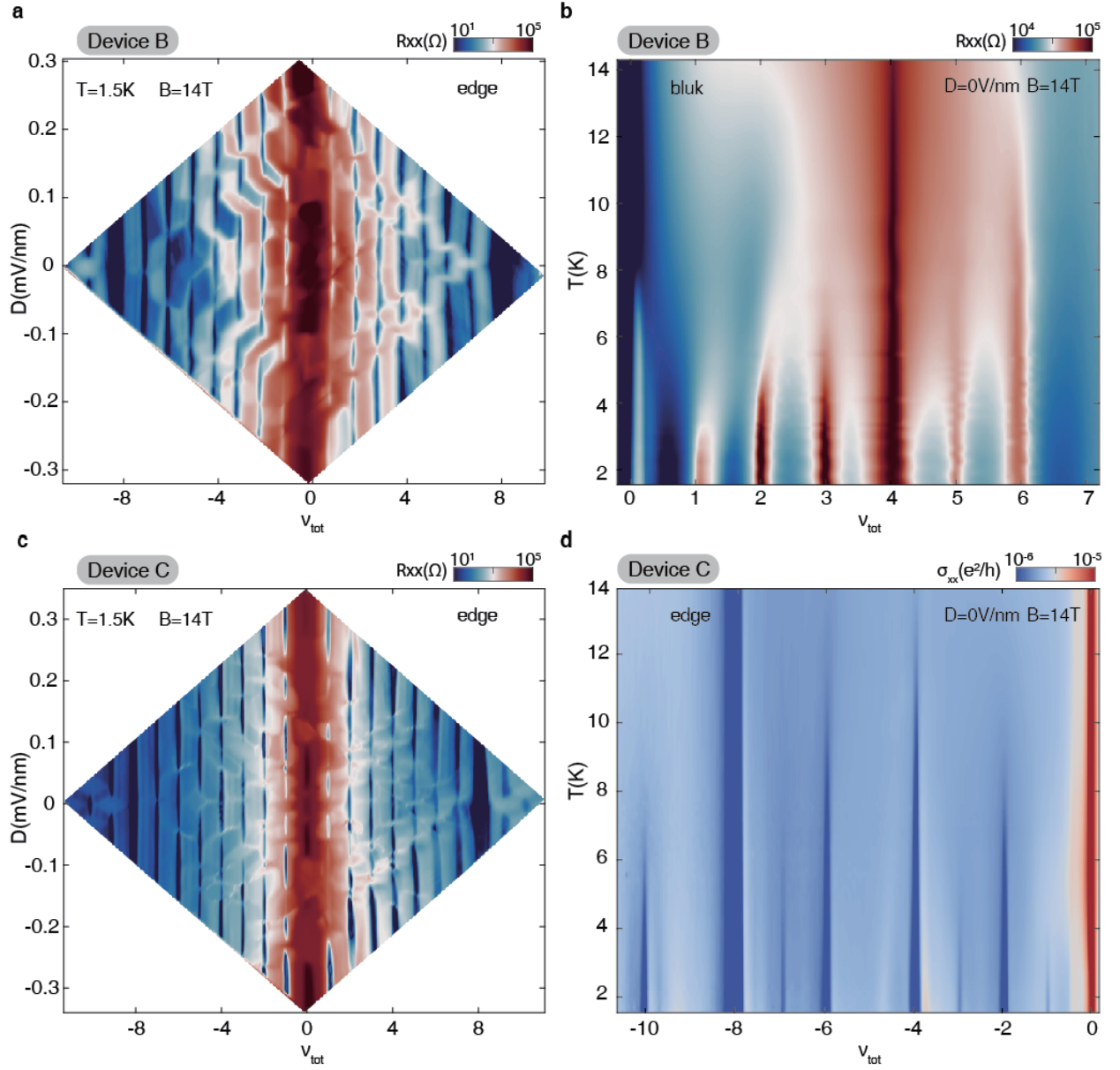


FIG. S3. the *8times8* structure and temperature dependence of ECs in other devices. **a-c**, Longitudinal resistance R_{xx} of TDBG at $B = 14\text{ T}$ and $T = 1.5\text{ K}$, versus ν_{tot} and D in device A(a) and device B(c). **b**, Bulk resistance $R_{xx-bulk}$ versus T and ν_{tot} at $D=0\text{ V/nm}$ in device A. **d**, Longitudinal conductance σ_{xx} versus T and ν_{tot} at $D=0\text{ V/nm}$ in device B.

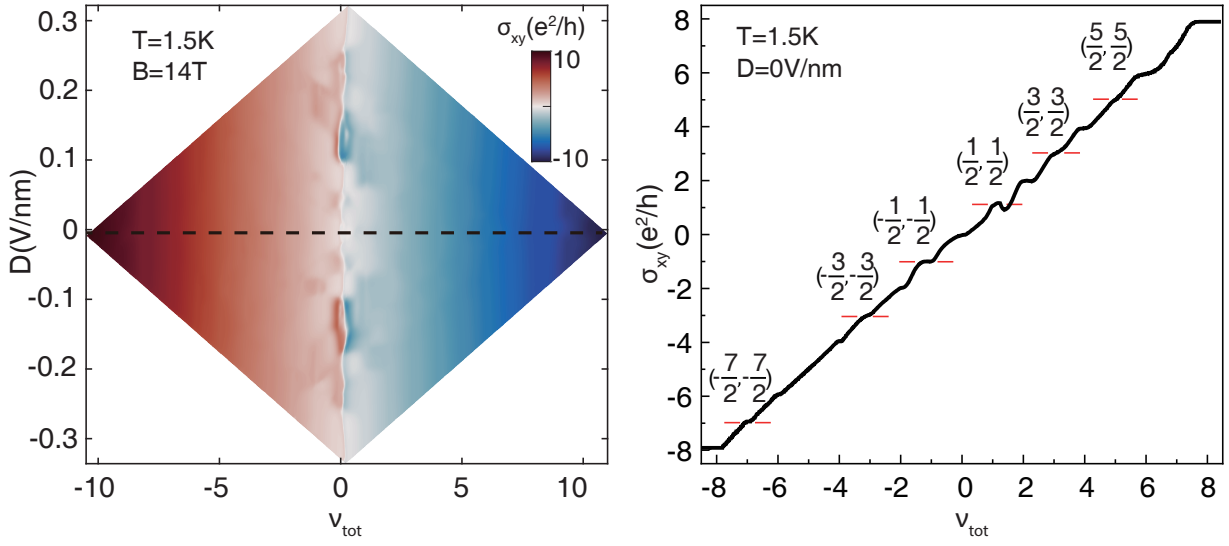


FIG. S4. σ_{xy} of all ECs. **a**, σ_{xy} versus D and ν_{tot} at $B = 14$ T and $T = 1.5$ K. **b**, The linecut of (a) along the black dashed line at $D = 0$ V/nm. A series of anomalous states at $\nu_{tot} = -7, -3, -1, 1, 3$ and 5 are marked by red crosses with quantized Hall conductivity and accompanying vanishing longitudinal conductivity (see maintext Fig. 2a). Given that the tunneling is negligible here, this phenomenon implies the emergence of a correlation energy gap due to many-body interactions. When both bilayers are half-filled, interlayer interactions prompt electrons in one bilayer and holes in the other to form magneto-excitons and condense into an incompressible superfluid: exciton condensate.

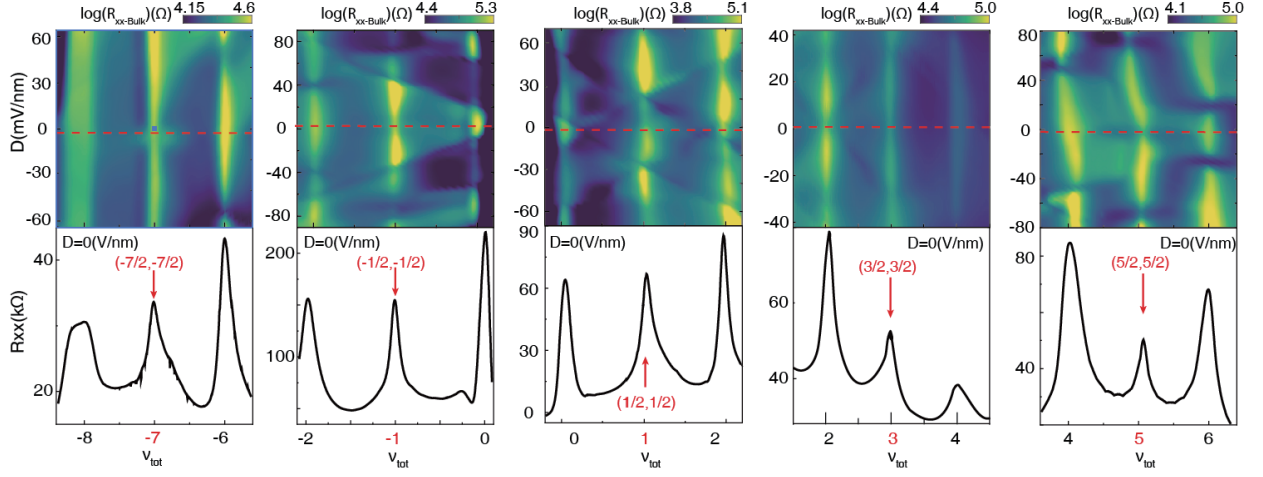


FIG. S5. All ECs at $D = 0$ V/nm. Bulk resistance $R_{xx-bulk}$ versus total filling factor ν_{tot} and displacement field D at $B = 14$ T around $D = 0$ V/nm. Each bottom panel is a linecut along the grey dashed line in the top panel, which tracks the equal topmost LL population in the two layers.

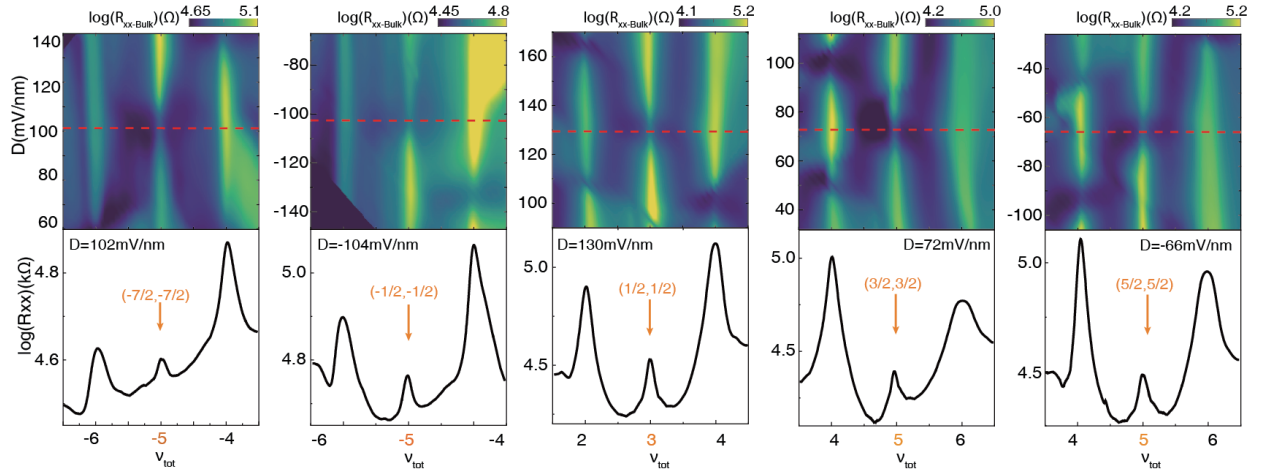


FIG. S6. All ECs at $D \neq 0$. Bulk resistance $R_{xx-bulk}$ versus total filling factor ν_{tot} and displacement field D at $B = 14$ T when $D \neq 0$. Each bottom panel is a linecut along the grey dashed line in the top panel, which tracks the equal topmost LL population in the two layers.

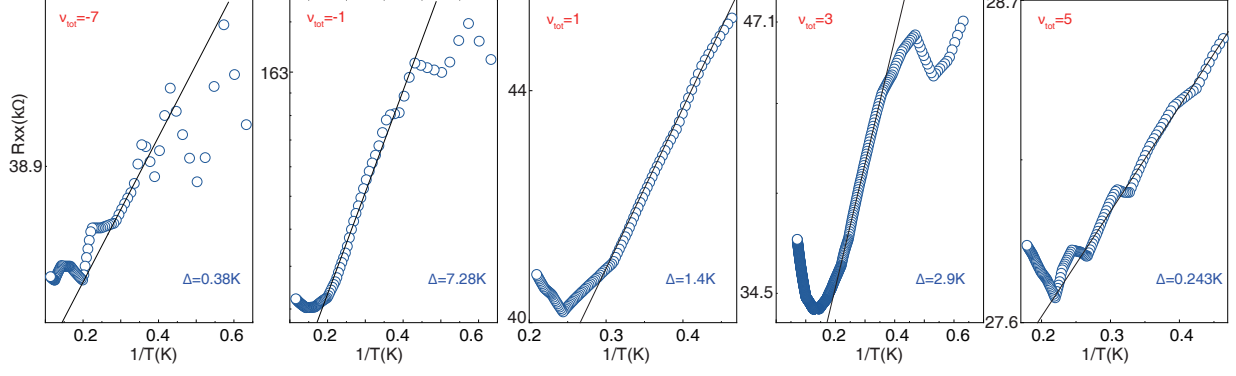


FIG. S7. Arrhenius Fits for all ECs at $\nu_{tot} = -7, -1, 1, 3, 5$. Logarithm of bulk resistance $\ln(R_{xx})$ versus $1/T$ at $D = 0\text{V/nm}$ at $\nu_{tot} = -7, -1, 1, 3, 5$.

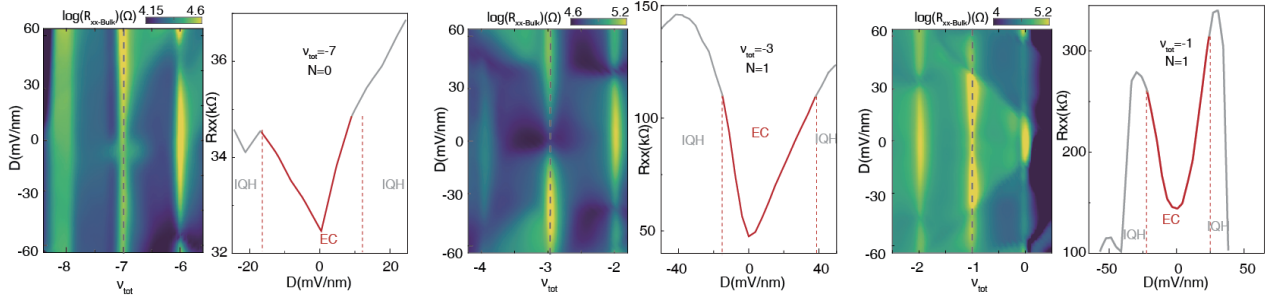


FIG. S8. Layer imbalance of ECs on hole side. $R_{xx-Bulk}$ as a function of D for the ECs at $\nu_{tot} = -7, -3, -1$ which correspond to $N = 0, 1$ and 1 LL, respectively. Red curve regions mark ECs and grey curves correspond to IQH regime.

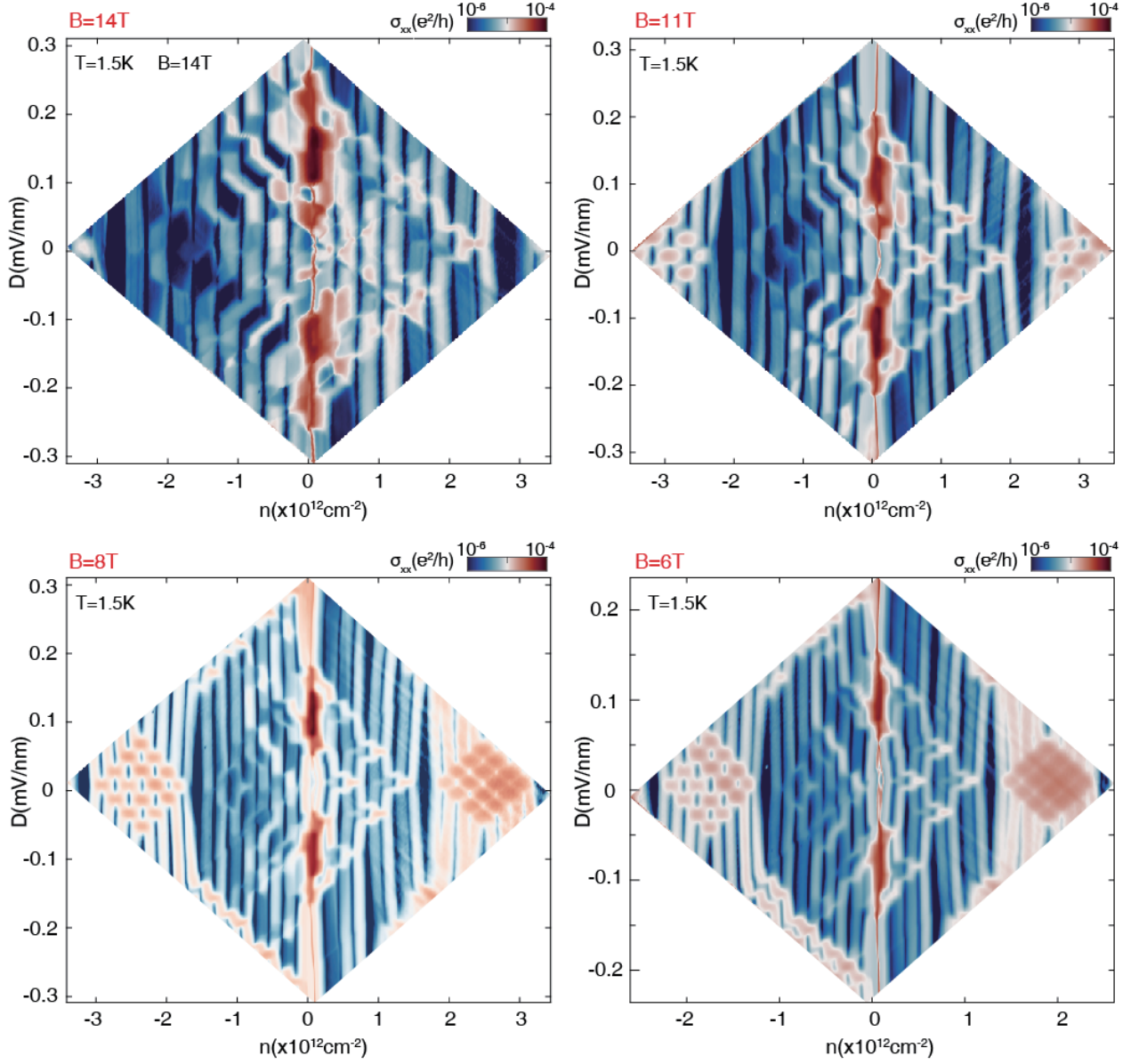


FIG. S9. ECs in the ‘8times8’ matrix at different magnetic fields The longitudinal conductivity σ_{xx} versus D and ν_{tot} at $T = 1.5$ K and $B = 14$ T, 11 T, 8 T, 6 T. when $B = 14$ T, ECs appearing at $\nu_{tot} = -7, -3, -1, 1, 3$ and 5 manifest as vanishing longitudinal conductivity states, and as the magnetic field weakens, these ECs gradually diminish, giving way to finite conductivity in these fillings.

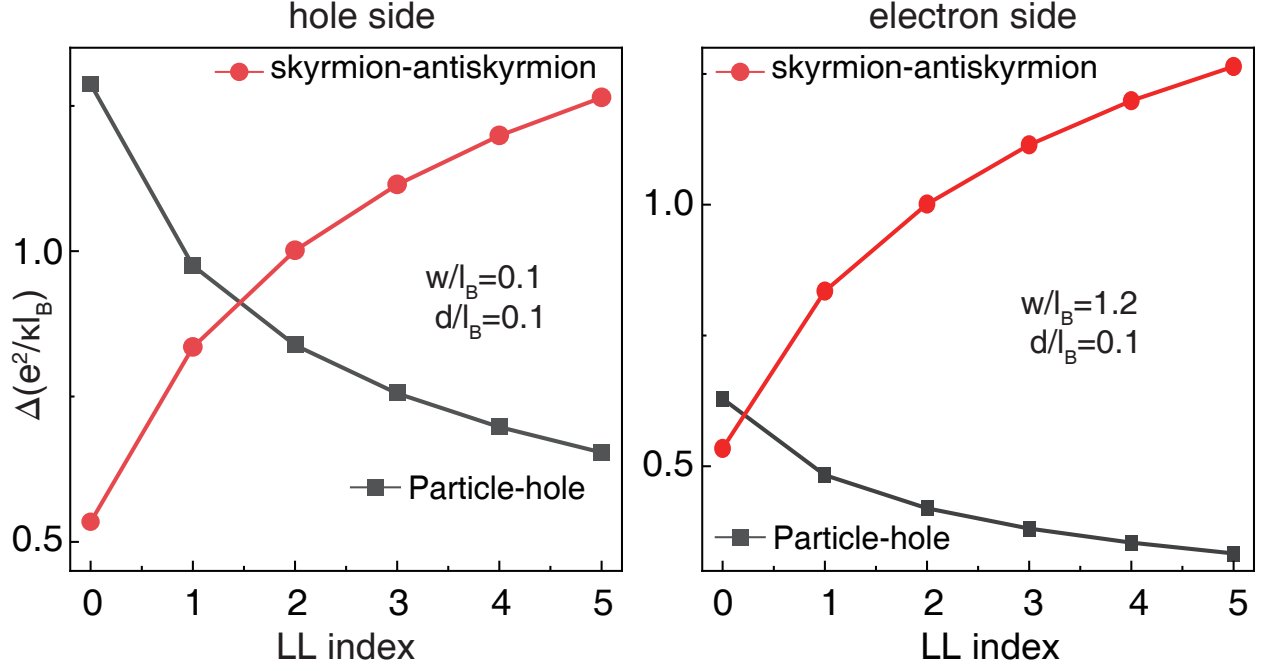


FIG. S10. The comparison between two types excitation gap with Landau level index on electron and hole sides. Theoretical calculations of energy gap for two types of excitations on hole and electron sides, at $d/l_B = 0.1$ and $D = 0$ V/nm. The spin-texture excitation energy increases with LL index while particle-hole excitation energy decreases with LL index. Their crossing points for hole and electron sides appear at different positions of LL index due to the screening strength increasing with total filling. The filled markers represent the lowest-energy excitations of ECs.